Geophysical Journal International

# Shear wave velocities in the upper mantle of the Western Alps: new constraints using array analysis of seismic surface waves

| | |
|---|---|
| Journal: | *Geophysical Journal International* |
| Manuscript ID | GJI-S-16-1044.R2 |
| Manuscript Type: | Research Paper |
| Date Submitted by the Author: | 19-Apr-2017 |
| Complete List of Authors: | Lyu, Chao; Institute of Geology and Geophysics Chinese Academy of Sciences,<br>Pedersen, Helle; Univ. Grenoble Alpes, ISTerre; CNRS, ISTerre<br>Paul, Anne; Université Grenoble Alpes, ISTerre<br>Zhao, Liang; Institute of Geology and Geophysics, Chinese Academy of Sciences, State Key Laboratory of Lithospheric Evolution<br>solarino, stefano; 5Istituto Nazionale di Geofisica e Vulcanologia, CNT |
| Keywords: | Surface waves and free oscillations < SEISMOLOGY, Continental margins: convergent < TECTONOPHYSICS, Europe < GEOGRAPHIC LOCATION |
| | |

# Shear wave velocities in the upper mantle of the Western Alps: new constraints using array analysis of seismic surface waves

Chao Lyu [1, 2, 3], Helle A. Pedersen[2, 3*], Anne Paul [2, 3], Liang Zhao [1*], Stefano Solarino[4], and the CIFALPS Working Group[†]

[1]State Key Laboratory of Lithospheric Evolution, Institute of Geology and Geophysics, Chinese Academy of Sciences, Beijing, China; zhaoliang@mail.iggcas.ac.cn.

[2]Univ. Grenoble Alpes, ISTerre, Grenoble, France; helle.pedersen@univ-grenoble-alpes.fr.

[3]CNRS, ISTerre, Grenoble, France.

[4] Istituto Nazionale di Geofisica e Vulcanologia, CNT, Genoa, Italy.

## SUMMARY

It remains challenging to obtain absolute shear wave velocities of heterogeneities of small lateral extension in the uppermost mantle. This study presents a cross section of Vs across the strongly heterogeneous 3-D structure of the western European Alps, based on array analysis of data from 92 broadband seismic stations from the CIFALPS experiment and from permanent networks in France and Italy. Half of the stations were located along a dense sub-linear array. Using a combination of these stations and off-profile stations, fundamental mode Rayleigh wave dispersion curves were calculated using a combined frequency-time beamforming approach. We calculated dispersion curves for seven arrays of approximately 100 km aperture and fourteen arrays of approximately 50 km aperture, the latter with the aim of obtaining a 2D vertical cross section of Vs beneath the western Alps. The dispersion curves were inverted for Vs(z), with crustal interfaces imposed from a previous receiver function study. The array approach proved feasible, as Vs(z) from independent arrays vary smoothly across the profile length. Results from the seven large arrays show that the shear velocity of the upper mantle beneath the European plate is overall low compared to AK135 with the lowest velocities in the internal part of the western Alps, and higher velocities east of the Alps beneath the Po plain. The 2-D Vs model is coherent with i) a ~100km thick eastward-dipping European lithosphere west of the Alps, ii) very high velocities beneath the Po plain, coherent with the presence of the Alpine (European) slab, and iii) a narrow low velocity anomaly beneath the core of the western Alps (from the Briançonnais to

† CIFALPS Working Group: Coralie Aubert, Marco G. Malusà, Qingchen Wang, Stéphane Guillot, Silvia Pondrelli, Simone Salimbeni, Stéphane Schwartz, Thierry Dumont, Tianyu Zheng, Rixiang Zhu

the Dora Maira massif), and approximately co-located with a similar anomaly observed in a recent teleseismic P-wave tomography. This intriguing anomaly is also supported by travel time variations of sub-vertically propagating body waves from two teleseismic events that are approximately located on the profile great circle.

**Key words**
Array analysis, surface waves, phase velocity, uppermost mantle, Alps

## 1 Introduction

The driving forces of tectonic deformation and associated surface processes and hazards in mountainous regions (topography building and subsequent erosion, landslides, earthquakes, etc.) are seated in the mantle, and possibly in small-scale convection of the upper mantle (e.g. Faccenna *et al.,* 2014). A better understanding of processes at play requires geodynamic modelling based on high-quality images on the structure and dynamics of the upper mantle. However seismic tomography is particularly challenging in mountainous areas due to strong lateral heterogeneities and therefore the need of particularly dense seismic networks. A challenge remains recovering high-resolution images of Vs, a key indicator of temperature and compositional heterogeneity, across 3-D, narrow, and strongly heterogeneous structures such as the western Alps.

The European Alps are part of the complex boundary zone between the European and African plates. They are the result of the Cretaceous to Paleogene subduction of the Tethyan ocean and the European continental margin beneath the Adriatic microcontinent, and the subsequent continental collision between the European and Adriatic paleomargins (e.g. Handy *et al.*, 2010; Dewey *et al.*, 1989 and references therein). The complex tectonic setting of the western Alps and their transition to the Apennines (arcuate shape, lateral change in subduction polarity with Adria being the upper plate in the Alps and the lower plate in the Apennines) results from a complex history including complex geometry of the paleotrench, lateral changes in the polarity of the subduction, rollback of the Apenninic slab leading to the opening of the Ligurian Sea and counterclockwise rotation of Adria (e.g. Jolivet and Faccenna, 2000; Malusà *et al.*, 2015). A specific point of interest is that the subduction complex of the western Alps, also including the eclogitized continental crust of the internal crystalline massifs, displays well preserved outcrops of (U)HP rocks attesting deep burial and exhumation of continental crust down to mantle depth (Chopin, 1984; Guillot *et al.*, 2009; Zhao *et al.*, 2015). Another point of interest is the potential role of the mantle in controlling the fast uplift of the External crystalline massifs, which include the highest summits of the Alps (e.g., the Mont Blanc), in the last 2 My (Fox *et al.*, 2015). This uplift has been partly explained by the breakoff of the Tethyan-European slab (Nocquet *et al.*, 2016) inferred from the seismic tomography of Lippitsch *et al.* (2003). However, a recent seismic tomography of the same region (Zhao *et al*., 2016a) suggests that the European slab is not broken off, and that a low-velocity anomaly exists in the lower lithosphere and asthenosphere beneath the core of the Western Alps. A high-resolution shear-wave imaging of the mantle structure of the Western Alps may provide key information complementing the body-wave model of Zhao *et al.* (2016a) to further understand the impact of mantle structure on surface processes and topographic evolution.

Regional surface wave tomographies based on two station measurements and full waveform inversion (e.g. Weidle and Maupin, 2008; Legendre *et al.*, 2012; Fichtner *et al.*, 2013; Zhu *et al.*, 2015; Meier *et al.*, 2016) have successfully provided large-scale images of the upper mantle beneath Europe. Array processing techniques using large arrays (a few hundred kilometres aperture) have already been used by many groups to obtain very well constrained upper mantle structure (e.g. Friederich, 1998; Pollitz, 1999; Bruneton *et al.*, 2004; De Barros *et al.*, 2008; Tang and Chen, 2008; Alvizuri and Tanimoto, 2011; Maupin, 2011; Salaün *et al.*, 2012; Pedersen *et al.*, 2013; Ikeda and Tsuji, 2014) and ambient noise tomography techniques are now standard for investigating crustal structure for the Alpine region (see Stehly *et al.*, 2009; Molinari *et al.*, 2015). While the usage of arrays is becoming standard for estimating great-circle deviations (e.g. Alsina and Snieder, 1996; Maupin, 2011; Foster *et al.*, 2014; Pedersen *et al.*, 2015), and has been used to improve two-station measurements (Baumont *et al.*, 2002; Bourova *et al.*, 2005; Kaviani *et al.*, 2007; Tanimoto and Prindle, 2007; Foster *et al.*, 2013), the usage of small arrays is rather sparse for investigating the lithosphere (e.g. Cotte *et al.*, 2002; Pedersen *et al.*, 2003). We here explore the complementary imaging opportunities given by array analysis of surface waves across the western Alps, using arrays with an aperture smaller than the wavelengths under study. A fundamental assumption behind this approach is that the observed phase velocities approximately correspond to the phase velocity of a tabular medium (‘structural velocity’, Wielandt, 1993) with interfaces at the same depth as those locally beneath the array within a laterally varying medium. This is a necessary condition to invert the observed phase velocities into a meaningful model. Through waveform modelling including multiple scattering, Bodin and Maupin (2008) explored differences between observed (array analysis) and structural velocities of fundamental mode Rayleigh waves within a 3-D structure (with a low velocity anomaly at 40 to 100 km depth). They demonstrated that also in a 3-D structure, and if events from different azimuths are used in the data analysis, the observed phase velocities are correctly located in the horizontal direction, and that the phase velocity change above the low velocity anomaly may be somewhat damped, depending on wavelength, array size and anomaly size.

We are here taking the next natural step in the array analysis: using it to provide a shear velocity cross-section of the Alps, using small adjoining arrays. As the measurements are sensitive to noise, care should be taken to not over-interpret individual array measurements. On the other hand, such measurements give valuable unique constraints of absolute shear velocities with a lateral resolution that is presently not possible to obtain from any other techniques. The CIFALPS array (Zhao *et al*., 2016b) was therefore designed as a test case for this approach, with a central, densely instrumented, profile well adapted for body wave tomography, receiver function analysis, etc., with additional sparse stations installed approximately 40 km from the central line. We additionally benefited from data from permanent stations on both sides of the CIFALPS line.

## 2 Data and Methods

*Data and preprocessing*

The CIFALPS (China-Italy-France Alps seismic survey, Zhao *et al*., 2016b) was a temporary broadband seismic network that operated for fourteen months between July 2012 and September 2013. In this study, we used vertical component data from 55 CIFALPS temporary broadband stations, with the addition of 37 neighbouring permanent stations from the RESIF network in France (network code FR; RESIF, 1995) and Italy (network codes GU, University of Genova, 1967; and IV, INGV Seismological Data Centre, 1997) for which continuous datastreams were available (see station configuration in Figure. 1). Approximately half (46) of the stations were located along a 320km long WSW-ENE transect with an interstation distance of approximately 5 km in the central part of the Alps, and 10 km in the external parts. Off-profile (45) stations were part of the array geometry with the aim of making it possible to perform array analysis. We later refer to the linear profile A-A' that follows the CIFALPS transect, also shown in Figure 1.

The initial dataset was composed of all worldwide events of magnitude 6 and more that were recorded during the CIFALPS experiment, with the addition of regional events (epicentral distance <20°) of magnitude 5.5 and more. Prior to further processing, we applied for each event data standard processing: removing mean and trend, applying zero-phase bandpass filter (0.005 Hz – 0.1 Hz), decimation and deconvolution from instrument response. Traces with easily identifiable instrumental problems such as spikes, poor signal to noise ratio and faulty components were automatically removed. Fig. S1 shows an example of a seismic section of filtered data.

All pre-processed data were subsequently filtered with phase-match filter (Levshin *et al.*, 1989) to extract the fundamental mode Rayleigh waves by a semi-automatic approach. We first calculated and visually inspected the output of multiple filter analysis of data from OGAG, a permanent station located near the center of the profile. The group velocity dispersion curve and the width of the applied time window (at least 300s) were chosen interactively and the output of the filter was also visually inspected. We only kept events for which the Rayleigh wave fundamental mode was clearly identifiable and separated from other arrivals, such as for example higher modes. For each accepted event, we then applied the filter to all stations, correcting for the difference in epicentral distance. The small interstation distances as compared to the epicentral distance justify this procedure, as the group velocity dispersion curve at different stations within the array is practically the same. In the event of lack of data or poor signal to noise ratio at OGAG, we used a neighbouring temporary station with high signal to noise ratio. For all events, we plotted seismic sections of all the filtered data in different period intervals to identify and if necessary manually discard data from stations with poor data quality. The final event dataset (see event configuration in Figure 2) after quality selection comprises 5 events with magnitude >=5.5 and epicentral distance < 20° and 93 events with magnitude >=6 and epicentral distance between 20° and 110°.

*Array analysis*

The data analysis was aimed at obtaining phase velocity dispersion curves, and subsequently estimates of 1-D Vs(z) profiles, beneath a set of arrays. Most array processing methods for teleseismic events are based on the hypothesis of plane incoming waves, and further assuming that averaging over a set of events with a good back azimuth distribution will suppress possible influence of diffraction outside the array. As shown in Figure 2, the azimuth distribution of the events we used was good, despite some dominance of events in the north-east quadrangle. In an area of laterally homogeneous crust and upper mantle structures, and in absence of scattering outside the array, increasing the array size reduces the measurement error. In a very heterogeneous area, such as the Alps, this effect is counterbalanced by an increase in coherent noise due to non-plane waves and local scattering. We therefore present results from two different array sizes: relatively large arrays (all shown in Figure 1, arrays A1-A7) that will indicate average dispersion over an area of approximately 100 km x 100 km, and a set of smaller arrays, a1-a14 of approximately 50 km x 50 km located on the north and south sides of the CIFALPS transect (all shown in Figure 5a, arrays a1-a14). The latter cover an area sufficiently small to make a cross section along the CIFALPS transect, and each takes into account the crustal structure obtained by receiver functions (Zhao *et al.*, 2015), as the lateral resolution of the two methods becomes comparable (and comparable to the width of the crustal blocks with laterally homogeneous structure).

The main steps of the array method are discussed briefly here; we refer to Pedersen *et al.* (2003) and supplementary material of Pedersen *et al.* (2013) for further detail. It is essentially a mixed time-frequency domain beamforming with an output relatively similar to that obtained by beamforming using for example f-k analysis (for a comparison, see Pedersen *et al.* (2015), but with a slightly better outlier control, and a frequency dependent smoothing of the phase).

The Rayleigh surface wave phase velocity of one array was measured in three main steps.

1. For each event *k,* the time delay $\Delta t_{ijk}(f)$ between each pair $(i, j)$ of stations in the array was measured as a function of frequency *f* using Wiener filtering. We use Wiener filtering to smooth the spectrum of the cross-correlation of the two signals by multiplying the cross-correlation with a Hanning window (centered on the time of maximum in the cross-correlation). One problem of this method is that the Hanning window must contain several oscillations of the longest period. On the other hand, applying short time windows will decrease the influence of noise. Considering the wide period interval used (15-100 s), different orders of the Hanning window were therefore adapted to different period intervals. We used 3 overlapping windows (periods 10s-50s, 40s-80s, 70s-100s) and calculated the phase of the smoothed spectrum in each window. In overlapping parts, we used a linear weighted average so that at each end point of the overlapping section, we ensured continuity with the neighbouring points. By this procedure, we obtained the smooth phase difference $\phi_{ijk}(f)$ and consequently the time delay $\Delta t_{ijk}(f)$ was calculated as ${\phi_{ijk}(f)}/{2\pi f}$. Note that due to the short interstation distance, there is no 2π uncertainty: incorrect phase unwrapping gives unrealistic, and therefore detectable, apparent interstation velocities.
2. Assuming a plane wave propagating across the array, for each event and at each frequency, we estimated the phase velocity $C_k(f)$ and backazimuth $\theta_k(f)$ by using the L1 norm to minimize the sum of the absolute time difference between predicted and observed time delays. It was then possible to calculate the interstation distance $D_k(f)$ projected onto the

slowness vector. The output of this step was, for each event and frequency, observed time delays associated with estimated projected interstation distances. Furthermore, events and frequencies for which the estimated velocity was outside the interval 2 km.s$^{-1}$ – 5 km.s$^{-1}$ or for which the data fit (L1 norm) was above 0.4 were rejected from further analysis.

3. For each frequency, $\left(D_k\left(f\right),\Delta t_{ijk}\left(f\right)\right)$ couples over all the events should fit a straight line through the origin, with the slope being the slowness at frequency *f*. We therefore calculated the best fitting slope, using the L1 norm. To further control outliers, we used only data points for which the coherency associated with the observed time delay was more than 0.9. The associated uncertainty was calculated as explained in Pedersen *et al.* (2003), where we used the median fit to the line for the uncertainty estimation, based on the velocity change incurred if the median fit was subtracted from the time delays predicted at the furthest distance. By combining information from different frequencies, we constituted the phase velocity dispersion curve and associated uncertainties between 15s and 100s period. An example, for array A2, is shown in Figure 3.

A bi-product of the analysis step 2 is that $\theta_k$(f) gives insight to the great circle deviation, i.e. the difference between the observed backazimuth $\theta_k$(f) and the great-circle between earthquake and the center of the array in question. We generally confirm previous results by Pedersen *et al.* (2015), Figure S2 which show that the average deviation over all events is 8°-10° for periods less than 30s, and decrease to a constant level (5°) which may in part be created by data uncertainty, at periods over 50s. Individual array observations and events did show a large scatter, which may be partly due to local structure, and partly due to noise in data. We do indeed have some observations of systematic changes of great circle deviations across the array. The average deviation and details on how this average was obtained is found in Supplementary Fig. S2, as well as three examples for individual earthquakes in Figure S3. A thorough discussion of great circle deviations and their dependency on station and source locations is beyond the scope of this work; we refer to Foster *et al.* (2014) and Pedersen *et al.* (2015) for in-depth studies on this subject.

*Inversion for shear velocity Vs(z)*

To invert the Rayleigh wave dispersion curves for S-wave velocity as a function of depth, we used an iterative, weighted inversion (Herrmann, 2013) which allows to define strong discontinuities as well as depth intervals with a smooth velocity model, through a smoothing parameter imposed by the user. The crustal model is constrained by receiver functions and gravity modelling along the CIFALPS transect (Zhao *et al.*, 2015), and by receiver functions at a larger scale (Lombardi *et al.*, 2008) so we imposed the layer thickness in the crust based on these studies while we imposed smooth velocity variations in the mantle. With good constraints on strong interfaces, we inverted for Vs only. Small remaining errors in interface depth would translate into slightly biased velocities immediately above and/or below them, and there is, even if interface depths are exact, a tradeoff between lower crustal and uppermost mantle velocities. We therefore only interpreted our final models below 80km depth. It was not possible to retrieve information on anisotropy, first because azimuthal variations of phase velocity could either be attributed to heterogeneities outside the array, and secondly because of data scatter.

Because the dispersion characterizes integration over a depth range of the velocity structure, the inversion problem is strongly non-unique and influenced by relatively subjective choices, whether the inversion method is linearized or nonlinear. We deliberately aimed at obtaining the simplest possible Vs(z) model whilst obtaining a reasonable data fit. The inversion therefore took place in two steps.

In the first inversion, we used a starting model made of (from top to bottom): (1) the initial crustal model described above, (2) a 200 km-thick constant velocity layer beneath Moho, (3) a number of 50 km-thick layers down to 700 km depth with initial velocities from AK135 (Kennett *et al.*, 1995). While the inverted model was, at best, resolved to 200 km depth, we inverted to 700 km depth to avoid the propagation of errors from the deep parts of the model into the resolved part. In this first inversion, we used 5 theoretical dispersion curves with identical crustal structures and different velocities in the upper mantle to set the initial shear velocities in the top 200 km of the mantle. Using this simple model, the first inversion refined the average shear velocity in the upper mantle, which was subsequently used in the starting model for the second inversion.

In the second inversion, we refined the 200 km-thick constant layer velocity of upper mantle structure into 5 km thick layers, and applied smoothing to how the velocities can evolve with depth. The same approach was used for the crust but adapting the thickness of the layers so as to respect the depth of the major interfaces. The convergence rate was variable for different dispersion curves, but due to the strong smoothing of the mantle velocities the inversion was stable also over many iterations. We iterated the inversion four times to obtain the final Vs(z) model.

Figure 3 illustrates the two steps. The observed dispersion curve (blue points with associated error bars in Fig. 3a) and constant velocity uppermost mantle dispersion curves (thin dashed black lines in Fig. 3a) made it possible to define an initial model (blue continuous curve in Fig. 3b) for the first inversion, which after inversion gave the input model (green continuous curve in Fig. 3b) for the second inversion. The equivalent dispersion curve (green line in Fig. 3a) was, in this case as for all the other arrays, a good first approximation to the observed dispersion curves, despite some systematic differences. The second inversion yielded a smooth and simple mantle model (red continuous curve in Fig. 3a), with a good fit to the observed dispersion curve.

## 3. Results

*Lateral variability of lithospheric structure from seven large aperture arrays*

The choice of the large aperture (~100 km) arrays was constrained by the station configuration, but mainly determined by present knowledge of the lithospheric structure of the Western Alps. The criteria were that the array should if possible 1) be located above a relatively homogeneous crustal structure as inferred from the receiver function model of Zhao *et al.* (2015); and 2) not be located above a strong lateral heterogeneity as determined by the P-wave upper mantle tomography by Zhao *et al*. (2016a) that integrates CIFALPS data. We finally identified seven useable arrays (A1-A7 in Figure 1, with Supplementary Table S1 showing the stations used for each large array).

For the inversion of dispersion curves from arrays A2, A3 and A7, we used the receiver function model computed by Zhao *et al.* (2015) along the CIFALPS transect. This model has a sub-horizontal Moho beneath those arrays. For arrays A1, A5 and A6 we used the crustal model of Lombardi *et al.* (2008). A4, located in an area including the Ivrea Body, represents a challenge as the crust and uppermost mantle have very strong heterogeneities across the array, including a vertical stack of crust-mantle-crust layers (Zhao *et al.*, 2015). For that array, we estimated an equivalent Moho depth of 47 km, based on lateral averages of the Zhao *et al.* (2015) model.

Figure 4 shows the seven dispersion curves and associated mantle models. These models are a first indication of large lateral variations in shear wave velocities in the study area. West of the Alps (A1, A2, A3), the average velocities in the uppermost mantle down to 100 km depth are compatible with previously observed seismic shear velocities in Phanerozoic Europe of approximately 4.4 $km.s^{-1}$ as observed in regional studies (e.g. Weidle and Maupin, 2008; Legendre *et al.*, 2012), excepted areas having undergone for example recent basaltic volcanism

(Meier *et al.*, 2016). We additionally observe that velocities decrease at depth. The exact thickness of the lithosphere is difficult to estimate using fundamental mode surface waves (e.g. Bartzsch *et al.*, 2011). However, our smoothed Vs(z) profiles are west of the Alps, they are compatible with a lithospheric thickness of approximately 100 km, as observed in other areas of Phanerozoic Europe or in regional studies using surface waves (e.g. Dost, 1990; Cotte *et al.*, 2002) and S-receiver functions (Geissler *et al.*, 2010). Artemieva *et al.* (2006) also provide lithospheric thicknesses of approximately 100 km beneath most of Phanerozoic Europe, based on global models such as Shapiro and Ritzwoller (2002), and on integrated modelling.

We observe high velocities east of the study region (A7, Po Plain), a result in agreement with models of a subducting slab beneath the Po plain (Kissling, 1993; Spakman *et al.*, 1993; Lippitsch *et al.*, 2003; Piromallo and Morelli, 2003). A4, A5 and A6, located in the central part of the western Alps, have associated Vs(z) that are very variable and complex (A5 and A6), exemplifying that the array size may not be adequate due to the small lateral scale of lithospheric heterogeneity in those areas. They do however give an indication of anomalously low mantle velocities beneath both A4 and A5, a feature that we shall further explore in the following section.

*2-D S-wave velocity cross-section along the CIFALPS transect from 14 small arrays*

The primary objective of this section is to obtain a cross section of shear wave velocities along the CIFALPS transect, based on phase velocity measurements in ~50 km aperture arrays. Decreasing array size implies a trade-off as the measurement error increases due to random noise but decreases with regards to scattering and interfering waves (non-plane wave fronts). The trade-off will vary along the transect, depending on the array size and heterogeneity of the local structure. After numerous tests, we chose to define 14 arrays, by using stations from the CIFALPS transect and at least two off-transect stations. Arrays a1-a5 were located south of the CIFALPS transect while arrays a6-a14 were located north of it. Figure 5a shows the geometry of 14 arrays, and Supplementary Table S1 lists the stations used for each array. As an additional quality check, we verified that the average dispersion curve over adequate selections of small arrays was compatible with the dispersion curve from the nearest and/or overlapping large array (see supplementary material Figure S4).

An extra advantage of using the small arrays is that their lateral extension makes it relevant to use information from receiver functions along the CIFALPS transect (Zhao *et al.*, 2015), as the scale of resolution for the two methods are approaching. We first attempted joint inversions of dispersion curves and receiver functions from nearby stations, but the individual receiver functions were of insufficient quality to allow for inversion beneath the central part of the Alps. In particular, the amplitude ratio between the converted P-to-S wave at Moho and the incident P wave was in several locations too high to be modeled with simple 1-D models, thereby inducing unrealistic velocity jumps at Moho. Late arrivals in the receiver functions, which we attribute to 3-D effects, additionally resulted in spurious mantle discontinuities. Finally, in the western and eastern parts of the transect, the receiver functions were influenced by strong resonance effects beneath the thick basins of SE France and of the Po plain. We therefore used the final model by Zhao *et al.* (2015) to define the depth to crustal interfaces. Within each crustal layer, we let Vs in the crust free to vary during the inversions, as the Vs in the crust was not constrained from receiver functions. Due to the conservative choices on model parametrisation and inversion approach, the errors and their changes with depth on these models are very similar to the ones shown in Figure 4.

Velocities in the lower crust and uppermost mantle should be interpreted with great caution due to the trade-off between crustal and upper mantle velocities. It is nevertheless noticeable that in the western part of the profile (from -130 to +20 km), the Vs is quite homogeneous and lower than 4.0 km/s suggesting that the lower crust beneath the western Alps is relatively felsic (e.g. Goffé *et al.*, 2003) as observed beneath Tibet (Mechie *et al.*, 2012). Eastward, beneath the internal Alps (+50 in Figure 5c), Vs increases up to 4.2 km/s. It can be either interpreted as an increase of the mafic component or an increase of the velocity with the increase of the metamorphic grade. Considering that the tip of the European lower crust is of the same composition as the western part, the Vs increase is compatible with the progressive eclogitisation (Zhao *et al.*, 2015) of a dominant felsic lower crust.

Figure 5 shows the output of the inversions in the form of a cross section, where the center of mass of each array is projected onto the A-A’ profile (see the geometry of small arrays a1-a14 in Figure 5a and station list is in Supplementary Material, Table S1). Figure 5b shows the topography along the profile AA’. As absolute Vs yields insight to the physical properties of the medium, we show both a cross section with absolute velocities (Figure 5c), and a cross section where, at each depth, we calculated variations in percent to the horizontal average (Figure 5d). The average Vs(z) is shown in Supplementary Fig. S4. This average Vs(z) is virtually identical whether we calculate the average over arrays a1-a14 or over four large arrays that cover approximately the same area (see Supplementary Fig. S4), indicating that the dispersion curves from the small arrays are not systematically biased even at long periods where the array size is approximately a fifth to a tenth of the wavelength. The representation in Figure 5d is equivalent to output from teleseismic body wave tomographies, which yield velocity variations with respect an unknown velocity model that is laterally homogeneous, but that varies with depth.

A first observation, as seen from Figure 5c, and as discussed in the beginning of this section, is the very good lateral continuity between the independent measurements of each array, which lends additional reliability to the data analysis and the associated quality control. In terms of structure, the main feature of Figure 5c is the decrease in seismic velocities below 100 km depth in the western part of the cross section, tentatively associated with the lithosphere-asthenosphere boundary and in agreement with the observations from arrays A1-A3 (see also previous section). It is tempting to interpret the deepening of the top of the low-velocity layer that is approximately parallel to the European Moho as an eastward dipping lithosphere-asthenosphere boundary, in agreement with the interpretation of a previous body wave tomography of the area (Lippitsch *et al.*, 2003), but this interpretation is supported by only two array measurements. Indeed, due to poor data quality for stations located in the Po plain, we only have two Vs(z) profiles available east of the Alps. On the other hand, the very high velocities (~5 $km.s^{-1}$) of the lithospheric mantle beneath the Po plain are well constrained in the inversions both in the two easternmost small arrays (a13 and a14), as well as in the larger array A7. A final observation is that very low velocities (< 4 $km.s^{-1}$) are visible in the deepest part of the model (z > 120km) below x = 50 km.

Figure 5d highlights additional features, and makes it possible to further understand the lateral variations. Previously available body wave tomographies in the area do not have sufficient station coverage to resolve the smaller scale features of our Vs section, but our results are in overall agreement with the higher resolution tomography by Zhao *et al*. (2016a), from which we extracted the cross section shown as background in Figure 5d. From west to east we observe limited lateral variations in the external Alps (a1-a9, km -150-0), a hitherto unknown strong low velocity anomaly in the western internal Alps below 120 km depth (a10-a12, km 0-50), and high velocities beneath the Po plain (a13-a14, km 90-150). The strong low velocity anomaly beneath the internal Western Alps is also present in the results of the P-wave travel time tomographies by Zhao *et al*. (2016a) and Lippitsch *et al.* (2003), with weak amplitude in the latter. The small discrepancy of the location of the strong low velocity anomaly between body wave and surface wave tomographies may be due to the fact that the Alps in this area has a 3-D geometry. Indeed, the surface wave models appear as located on the CIFALPS profile while in reality they are spatial averages over arrays shifted several km towards the north of the profile (see Figure 5a).

Additional input to the analysis comes from travel time delays of body waves. We selected two events for which P and/or S arrivals were clear, for which the incidence is sub-vertical, and which are located approximately on the great-circle through A-A'. Their locations are shown as blue stars in Figure 2. We chose the highest quality data among those available: SKS phase (incidence 7.5° to vertical, from the west), SKKS phase (incidence 6.5° to vertical, from the east), and PKIKP phase (incidence 1° to vertical, from the east). The travel time differences of these phases with respect to the westernmost station CT01 are shown in Figure 5e. These travel time delays are not corrected for crustal effects, but as shown in Figure 5e, predicted relative time delays of vertically propagating P waves through the Zhao *et al.* (2015) crustal model are modest (note that the delays include the effect of topography). Indeed, the effect of the very deep European Moho below the Ivrea body is counterbalanced by the presence of mantle material above. The observed travel time differences are therefore dominated by very early arrivals due to the presence of a high-velocity subduction slab beneath the eastern part of the array as known from several P-wave tomographies (e.g. Lippitsch *et al.*, 2003; Piromallo and Morelli, 2003). The S-wave advance is surprisingly large, but clear in the seismic traces (Figure 5e). The effect of the anomalously low velocities beneath the internal Alps (approximately km 0-50 on the A-A' profile) is observed in the S-wave relative travel-times as a slight positive anomaly added on top of the large negative anomaly. While the data at hand does not allow for a depth inversion, the eastwards shift of this anomaly for the event located west of the array, and westwards shift for the event located east of the array is compatible with a mantle origin of the delays.

## 4. **Conclusions**

The present study demonstrates that array analysis, using arrays of ~50 km aperture, is indeed possible for fundamental mode Rayleigh waves and yields stable results across an extremely heterogeneous 3-D structure. This approach makes it possible to estimate absolute Vs over length scales of approximately the aperture of the array, and contains complementary information to other imaging methods, in particular receiver functions and P-wave tomography, and to regional surface wave studies. Due to the small size of the array as compared to the wavelengths under consideration, caution must be taken to avoid that spurious oscillations in the phase velocity dispersion curve has a significant influence on the inversion results. We therefore recommend firstly to take a conservative inversion approach of the dispersion curves, and secondly that the interpretations should be based on several arrays rather than on individual ones. Such strict considerations can probably be relaxed in less heterogeneous structures than that of the western Alps. In simpler structures, it may also be feasible to do fully joint inversions of receiver functions from individual or small groups of stations with array based dispersion curves. In terms of array geometry, the combination in CIFALPS of a dense linear array with off-profile stations in an approximately regular grid is an efficient setup, and realistic in terms of the additional number of stations required off profile.

In terms of deep Alpine structure, we highlight three main results:

1) The Vs(z) profiles are coherent with an approximately 100 km thick European lithosphere, in line with observations in other areas of Phanerozoic Europe unaffected by recent volcanism. Our results show dip values of the European lithosphere-asthenosphere boundary that are coherent with the Moho dip measured from controlled-source seismology and receiver function analysis (e.g. Nicolas *et al.*, 1990; Waldhauser *et al.*, 1998; Spada *et al.*, 2013; Zhao *et al.*, 2015).
2) Absolute Vs is high in the upper mantle beneath the Po plain, due to presence of the subducted Alpine slab, in agreement with both Vs models from full-waveform inversion (Zhu *et al.*, 2012; Fichtner and Villaseñor, 2015) and Vp perturbation models from travel-time tomography (e.g. Lippitsch *et al.*, 2003; Piromallo and Morelli, 2003; Zhao *et al.*, 2016a).
3) Our Vs(z) profiles confirm the results of teleseismic P-wave tomography (Zhao *et al.*, 2016a) showing anomalously low velocities in the upper mantle beneath the uplifting core of the western Alps. The possible relationships between such low velocity anomalies and uplift at the surface would require further investigation by mantle flow modelling. On the other hand, it is unlikely that such low velocities and related surface uplift are related to slab break-off, as suggested instead by Lippitsch *et al.* (2003).

**Acknowledgements**

The seismic data of the CIFALPS experiment are archived at the data center of the Seismic Array Laboratory, Institute of Geology and Geophysics, Chinese Academy of Sciences, and are freely available at the data center of the French Seismologic and Geodetic Network (RESIF; http://www.resif.fr/). We are most grateful to the operators of permanent broadband seismic arrays of European countries who make their data freely available through the EIDA (European Integrated Data Archive, http://www.orfeus-eu.org/eida/eida.html). And constructive reviews from two anonymous reviewers were greatly appreciated. The CIFALPS project is funded by the State Key Laboratory of Lithospheric Evolution, China, the National Natural Science Foundation of China (Grant 41625016) and by a grant from Labex OSUG@2020 (Investissements d'avenir –

ANR10 LABX56, France).

## References

Alsina, D. & Snieder, R., 1996. Constraints on the velocity structure beneath the Tornquist-Teisseyre Zone from beam-forming analysis, *Geophys. J. Int.,* 126**,** 205-218.

Alvizuri, C. & Tanimoto, T., 2011. Azimuthal anisotropy from array analysis of Rayleigh waves in Southern California, *Geophys. J. Int.,* 186**,** 1135-1151.

Artemieva, I.M., Thybo, H. & Kaban, M.K., 2006. Deep Europe today: geophysical synthesis of the upper mantle structure and lithospheric processes over 3.5 Ga, *Geol. Soc. London Mem.,* 32**,** 11-41.

Bartzsch, S., Lebedev, S. & Meier, T., 2011. Resolving the lithosphere–asthenosphere boundary with seismic Rayleigh waves, *Geophys. J. Int.,* 186**,** 1152-1164.

Baumont, D., Paul, A., Zandt, G., Beck, S.L. & Pedersen, H., 2002. Lithospheric structure of the central Andes based on surface wave dispersion, *J. Geophys. Res. Solid Earth,* 107.

Bodin, T. & Maupin, V., 2008. Resolution potential of surface wave phase velocity measurements at small arrays, *Geophys. J. Int.,* 172**,** 698-706.

Bourova, E., Kassaras, I., Pedersen, H.A., Yanovskaya, T., Hatzfeld, D. & Kiratzi, A., 2005. Constraints on absolute S velocities beneath the Aegean Sea from surface wave analysis, *Geophys. J. Int.,* 160**,** 1006-1019.

Bruneton, M., Pedersen, H.A., Vacher, P., Kukkonen, I.T., Arndt, N.T., Funke, S., Friederich, W., Farra, V. & Group, S.S.T.W., 2004. Layered lithospheric mantle in the central Baltic Shield from surface waves and xenolith analysis, *Earth Planet. Sci. Lett.,* 226**,** 41-52.

Chopin, C., 1984. Coesite and pure pyrope in high-grade blueschists of the Western Alps: a first record and some consequences, *Contrib Mineral Petrol.,* 86**,** 107-118.

Cotte, N., Pedersen, H. & Group, T.W., 2002. Sharp contrast in lithospheric structure across the Sorgenfrei–Tornquist Zone as inferred by Rayleigh wave analysis of TOR1 project data, *Tectonophysics,* 360**,** 75-88.

De Barros, L., Pedersen, H.A., Métaxian, J.-P., Valdés-Gonzalez, C. & Lesage, P., 2008. Crustal structure below Popocatépetl Volcano (Mexico) from analysis of Rayleigh waves, *J. Volcanol. Geotherm. Res.,* 170**,** 5-11.

Dewey, J.F., Helman, M.L., Knott, S.D., Turco, E. & Hutton, D.H.W., 1989. Kinematics of the western Mediterranean, *Geol. Soc. London Spec. Publ.,* 45**,** 265-283.

Dost, B., 1990. Upper mantle structure under western Europe from fundamental and higher mode surface waves using the NARS array, *Geophys. J. Int.,* 100**,** 131-151.

Dziewonski, A.M. & Anderson, D.L., 1981. Preliminary reference Earth model, *Phys. Earth Planet. In.,* 25**,** 297-356.

Faccenna, C., Becker, T.W., Auer, L., Billi, A., Boschi, L., Brun, J.P., Capitanio, F.A., Funiciello, F., Horvàth, F., Jolivet, L., Piromallo, C., Royden, L., Rossetti, F. & Serpelloni, E., 2014. Mantle dynamics in the Mediterranean, *Rev. Geophys.,* 52**,** 283-332.

Fichtner, A., Trampert, J., Cupillard, P., Saygin, E., Taymaz, T., Capdeville, Y. & Villasenor, A., 2013. Multiscale full waveform inversion, *Geophys. J. Int.,* 194**,** 534-556.

Fichtner, A. & Villaseñor, A., 2015. Crust and upper mantle of the western Mediterranean–Constraints from full-waveform inversion, *Earth Planet. Sci. Lett.,* 428**,** 52-62.

Foster, A., Ekström, G. & Hjörleifsdóttir, V., 2014. Arrival-angle anomalies across the USArray Transportable Array, *Earth Planet. Sci. Lett.,* 402**,** 58-68.

Foster, A., Ekström, G. & Nettles, M., 2013. Surface wave phase velocities of the Western United States from a two-station method, *Geophys. J. Int.***,** ggt454.

Fox, M., Herman, F., Kissling, E. & Willett, S.D., 2015. Rapid exhumation in the Western Alps driven by slab detachment and glacial erosion, *Geology,* 43**,** 379-382.

Friederich, W., 1998. Wave-theoretical inversion of teleseismic surface waves in a regional network: phase-velocity maps and a three-dimensional upper-mantle shear-wave-velocity model for southern Germany, *Geophys. J. Int.,* 132**,** 203-225.

Geissler, W.H., Sodoudi, F. & Kind, R., 2010. Thickness of the central and eastern European lithosphere as seen by S receiver functions, *Geophys. J. Int.,* 181**,** 604-634.

Goffé, B., Bousquet, R., Henry, P. & Le Pichon, X., 2003. Effect of the chemical composition of the crust on the metamorphic evolution of orogenic wedges, *J. Metamorph. Geol.,* 21**,** 123-141.

Guillot, S., Hattori, K., Agard, P., Schwartz, S. & Vidal, O., 2009. Exhumation Processes in Oceanic and Continental Subduction Contexts: A Review. *in Subduction Zone Geodynamics*, pp. 175-205, eds. Lallemand, S. & Funiciello, F. Springer Berlin Heidelberg, Berlin, Heidelberg.

Handy, M.R., M. Schmid, S., Bousquet, R., Kissling, E. & Bernoulli, D., 2010. Reconciling plate-tectonic reconstructions of Alpine Tethys with the geological–geophysical record of spreading and subduction in the Alps, *Earth-Sci. Rev.,* 102**,** 121-158.

Herrmann, R.B., 2013. Computer Programs in Seismology: An Evolving Tool for Instruction and Research, *Seismol. Res. Lett.,* 84**,** 1081.

INGV Seismological Data Centre, 1997. Rete Sismica Nazionale (RSN), Istituto Nazionale di Geofisica e Vulcanologia (INGV), Italy, doi:10.13127/SD/X0FXnH7QfY.

Ikeda, T. & Tsuji, T., 2014. Azimuthal anisotropy of Rayleigh waves in the crust in southern Tohoku area, Japan, *J. Geophys. Res. Solid Earth,* 119**,** 8964-8975.

Jolivet, L. & Faccenna, C., 2000. Mediterranean extension and the Africa-Eurasia collision, *Tectonics,* 19**,** 1095-1106.

Kaviani, A., Paul, A., Bourova, E., Hatzfeld, D., Pedersen, H. & Mokhtari, M., 2007. A strong seismic velocity contrast in the shallow mantle across the Zagros collision zone (Iran), *Geophys. J. Int.,* 171**,** 399-410.

Kennett, B., Engdahl, E. & Buland, R., 1995. Constraints on seismic velocities in the Earth from traveltimes, *Geophys. J. Int.,* 122**,** 108-124.

Kissling, E., 1993. Deep structure of the Alps—what do we really know?, *Phys. Earth Planet. In.,* 79**,** 87-112.

Legendre, C.P., Meier, T., Lebedev, S., Friederich, W. & Viereck-Götte, L., 2012. A shear wave velocity model of the European upper mantle from automated inversion of seismic shear and surface waveforms, *Geophys. J. Int.,* 191**,** 282-304.

Levshin, A., Yanovskaya, T., Lander, A., Bukchin, B., Barmin, M., Ratnikova, L. & Its, E., 1989. Seismic surface waves in a laterally inhomogeneous Earth, *Modern Approaches Geophys.,* 9**,** 131-169.

Lippitsch, R., Kissling, E. & Ansorge, J., 2003. Upper mantle structure beneath the Alpine orogen from high-resolution teleseismic tomography, *J. Geophys. Res.-Solid Earth,* 108**,** 15.

Lombardi, D., Braunmiller, J., Kissling, E. & Giardini, D., 2008. Moho depth and Poisson's ratio in the Western-Central Alps from receiver functions, *Geophys. J. Int.,* 173**,** 249-264.

Malusà, M.G., Faccenna, C., Baldwin, S.L., Fitzgerald, P.G., Rossetti, F., Balestrieri, M.L., Danišík, M., Ellero, A., Ottria, G. & Piromallo, C., 2015. Contrasting styles of (U)HP rock exhumation along the Cenozoic Adria-Europe plate boundary (Western Alps, Calabria, Corsica), *Geochem. Geophys. Geosyst.,* 16**,** 1786-1824.

Maupin, V., 2011. Upper-mantle structure in southern Norway from beamforming of Rayleigh wave data presenting multipathing, *Geophys. J. Int.,* 185**,** 985-1002.

Mechie, J., Yuan, X., Schurr, B., Schneider, F., Sippl, C., Ratschbacher, L., Minaev, V., Gadoev, M., Oimahmadov, I., Abdybachaev, U., Moldobekov, B., Orunbaev, S. & Negmatullaev, S., 2012. Crustal and uppermost mantle velocity structure along a profile across the Pamir and southern Tien Shan as derived from project TIPAGE wide-angle seismic data, *Geophys. J. Int.,* 188**,** 385-407.

Meier, T., Soomro, R.A., Viereck, L., Lebedev, S., Behrmann, J.H., Weidle, C., Cristiano, L. & Hanemann, R., 2016. Mesozoic and Cenozoic evolution of the Central European lithosphere, *Tectonophysics*.

Molinari, I., Argnani, A., Morelli, A. & Basini, P., 2015. Development and testing of a 3D seismic velocity model of the Po Plain sedimentary basin, Italy, *Bull. Seismol. Soc. Am.,* 105**,** 753-764.

Nicolas, A., Hirn, A., Nicolich, R. & Polino, R., 1990. Lithospheric wedging in the western Alps inferred from the ECORS-CROP traverse, *Geology,* 18**,** 587-590.

Nocquet, J.-M., Sue, C., Walpersdorf, A., Tran, T., Lenôtre, N., Vernant, P., Cushing, M., Jouanne, F., Masson, F. & Baize, S., 2016. Present-day uplift of the western Alps, *Sci. Rep.,* 6.

Pedersen, H.A., Boué, P., Poli, P. & Colombi, A., 2015. Arrival angle anomalies of Rayleigh waves observed at a broadband array: a systematic study based on earthquake data, full waveform simulations and noise correlations, *Geophys. J. Int.,* 203**,** 1626-1641.

Pedersen, H.A., Coutant, O., Deschamps, A., Soulage, M. & Cotte, N., 2003. Measuring surface wave phase velocities beneath small broad-band arrays: tests of an improved algorithm and application to the French Alps, *Geophys. J. Int.,* 154**,** 903-912.

Pedersen, H.A., Debayle, E. & Maupin, V., 2013. Strong lateral variations of lithospheric mantle beneath cratons – Example from the Baltic Shield, *Earth Planet. Sci. Lett.,* 383**,** 164-172.

Piromallo, C. & Morelli, A., 2003. P wave tomography of the mantle under the Alpine-Mediterranean area, *J. Geophys. Res. Solid Earth,* 108.

Pollitz, F.F., 1999. Regional velocity structure in northern California from inversion of scattered seismic surface waves, *J. Geophys. Res. Solid Earth,* 104**,** 15043-15072.

RESIF, 1995. RESIF-RLBP French Broad-band network, RESIF-RAP strong motion network and other seismic stations in metropolitan France, RESIF – Réseau sismologique & géodésique français, doi:10.15778/RESIF.FR.

Salaün, G., Pedersen, H.A., Paul, A., Farra, V., Karabulut, H., Hatzfeld, D., Papazachos, C., Childs, D.M., Pequegnat, C. & Team, S., 2012. High-resolution surface wave tomography beneath the Aegean-Anatolia region: constraints on upper-mantle structure, *Geophys. J. Int.,* 190**,** 406-420.

Shapiro, N.M. & Ritzwoller, M.H., 2002. Monte-Carlo inversion for a global shear-velocity model of the crust and upper mantle, *Geophys. J. Int.,* 151**,** 88-105.

Spada, M., Bianchi, I., Kissling, E., Agostinetti, N.P. & Wiemer, S., 2013. Combining controlled-source seismology and receiver function information to derive 3-D Moho topography for Italy, *Geophys. J. Int.,* 194**,** 1050-1068.

Spakman, W., van der Lee, S. & van der Hilst, R., 1993. Travel-time tomography of the European-Mediterranean mantle down to 1400 km, *Phys. Earth Planet. In.,* 79**,** 3-74.

Stehly, L., Fry, B., Campillo, M., Shapiro, N., Guilbert, J., Boschi, L. & Giardini, D., 2009. Tomography of the Alpine region from observations of seismic ambient noise, *Geophys. J. Int.,* 178, 338-350.

Tang, Q. & Chen, L., 2008. Structure of the crust and uppermost mantle of the Yanshan Belt and adjacent regions at the northeastern boundary of the North China Craton from Rayleigh Wave Dispersion Analysis, *Tectonophysics,* 455, 43-52.

Tanimoto, T. & Prindle, K., 2007. Surface wave analysis with beamforming, *Earth, Planets Space.,* 59, 453-458.

University of Genova, 1967. Regional Seismic Network of North Western Italy, International Federation of Digital Seismograph Networks, Other/Seismic Network, doi:10.7914/SN/GU.

Waldhauser, F., Kissling, E. & Ansorge, J., 1998. Three dimensional interface modelling with two-dimensional seismic data: the Alpine crust-mantle boundary, *Geophys. J. Int.,* 135, 264-278.

Weidle, C. & Maupin, V., 2008. An upper-mantle S-wave velocity model for Northern Europe from Love and Rayleigh group velocities, *Geophys. J. Int.,* 175, 1154-1168.

Wielandt, E., 1993. Propagation and structural interpretation of non-plane waves, *Geophys. J. Int.,* 113, 45-53.

Zhao, L., Paul, A., Guillot, S., Solarino, S., Malusà, M.G., Zheng, T., Aubert, C., Salimbeni, S., Dumont, T. & Schwartz, S., 2015. First seismic evidence for continental subduction beneath the Western Alps, *Geology,* 43, 815-818.

Zhao, L., Paul, A., Malusà, M.G., Xu, X., Zheng, T., Solarino, S., Guillot, S., Schwartz, S., Dumont, T., Salimbeni, S., Aubert, C., Pondrelli, S., Wang, Q. & Zhu, R., 2016a. Continuity of the Alpine slab unraveled by high-resolution P wave tomography, *J. Geophys. Res. Solid Earth*, 121.

Zhao, L., Paul, A., Solarino, S., RESIF, 2016b. Seismic network YP: CIFALPS temporary experiment (China-Italy-France Alps seismic transect); RESIF - Réseau Sismologique et géodésique Français. https://doi.org/10.15778/RESIF.YP2012

Zhu, H., Bozdag, E., Peter, D. & Tromp, J., 2012. Structure of the European upper mantle revealed by adjoint tomography, *Nature Geosci,* 5, 493-498.

Zhu, H., Bozdağ, E. & Tromp, J., 2015. Seismic structure of the European upper mantle based on adjoint tomography, *Geophys. J. Int.,* 201, 18-52.

# Figure captions

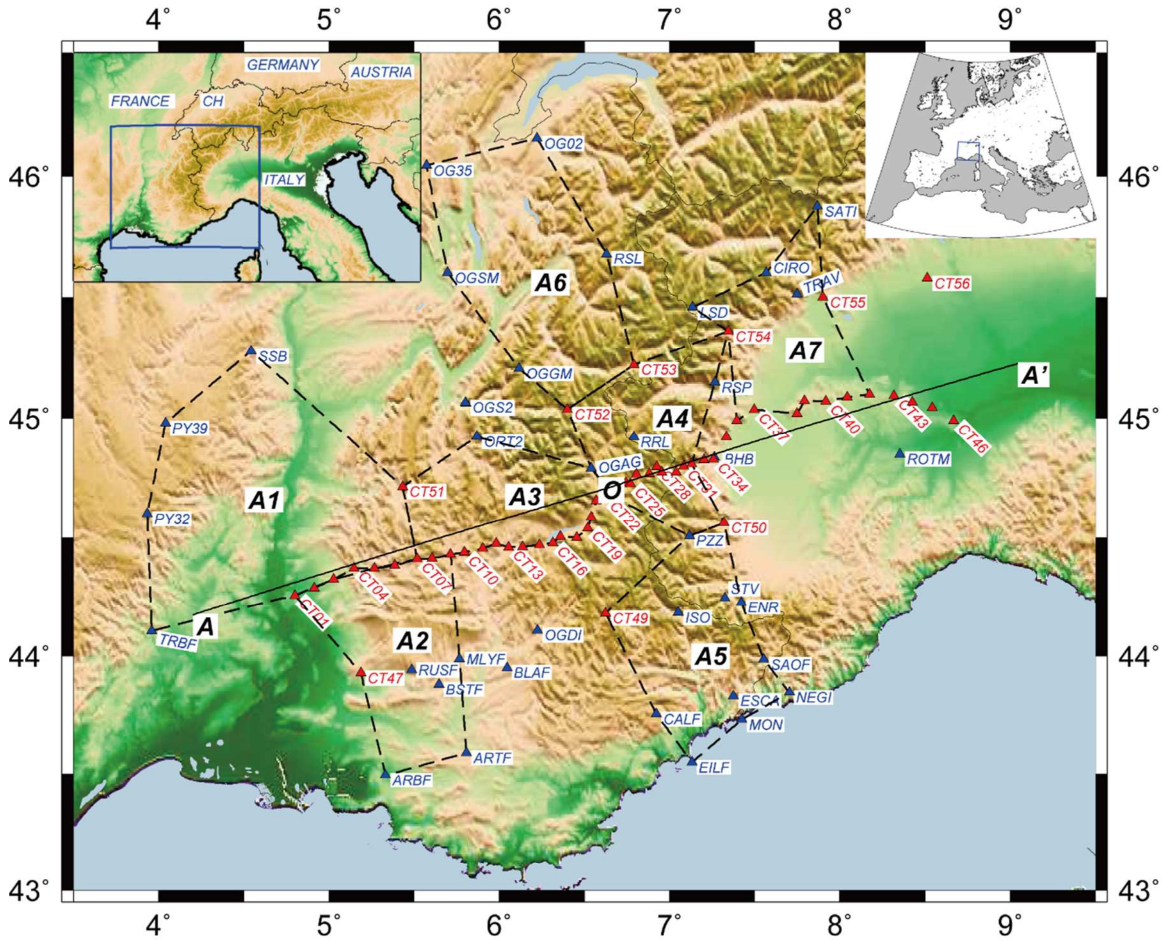


Figure 1. Map of seismic stations and large arrays. CIFALPS and permanent stations are shown as red and blue triangles respectively. Groups of stations connected by black dashed lines are the large arrays, numbered A1-A7. The continuous black line shows profile AA'. The origin of distance measurements along AA' (x = 0 km) is shown by O. CH：Switzerland.

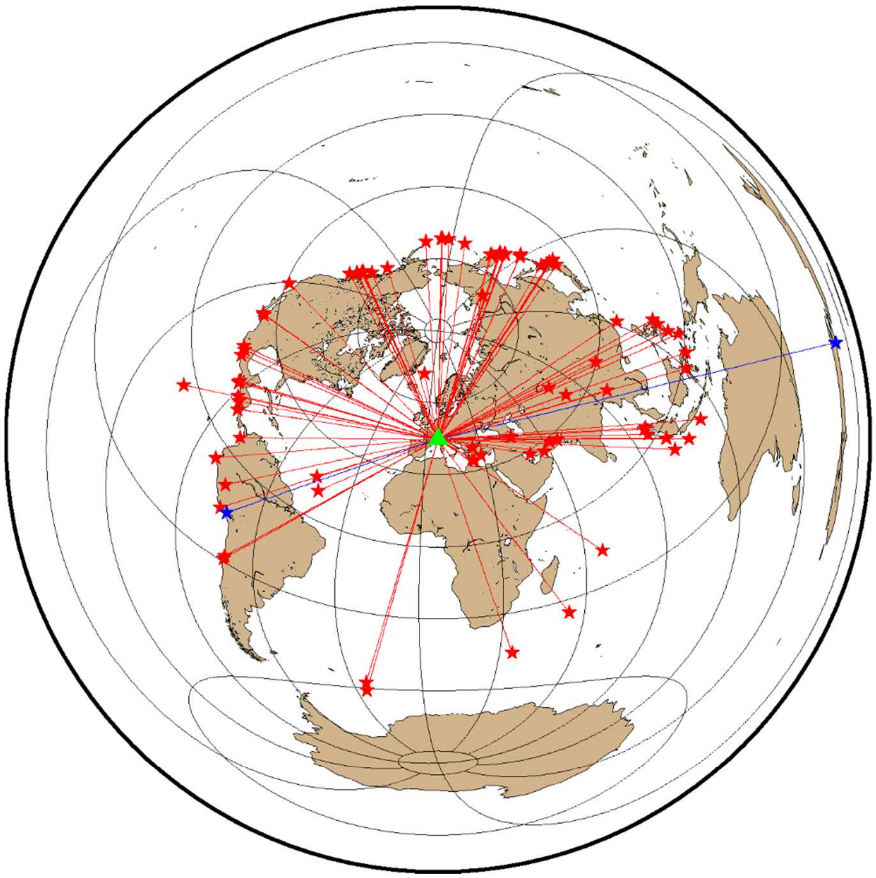

Figure 2. Earthquake map (Lambert azimuthal equal-area projection). We used 98 seismic events (red stars) to calculate phase velocity dispersion curves. The green triangle indicates the center of the CIFALPS array. Great-circles between events and the center of the array are shown with red lines. The blue stars refer to events for which travel time delays of body waves are shown in Figure 5e.

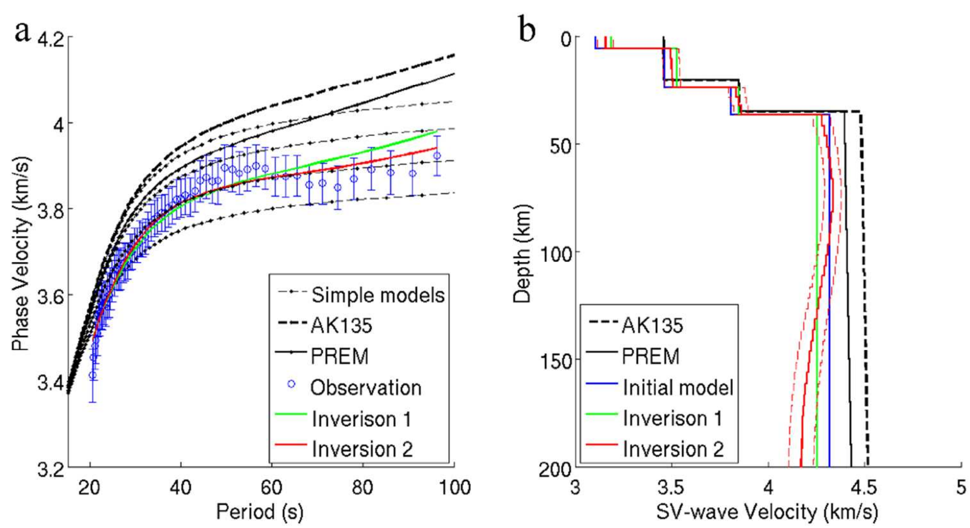


Figure 3. Example of inversion strategy (array A2). (a) Dispersion curves (fundamental mode

Rayleigh waves). Blue: observed phase velocity and associated error bars. Green: Theoretical dispersion curve for the model obtained in Inversion 1 (200 km thick constant-velocity layer in the upper mantle). Red: Theoretical dispersion curve for the final model obtained in Inversion 2, corresponding to our final model. Thick dashed black line: dispersion curve for AK135. Thick solid black line: dispersion curve for PREM (Dziewonski and Anderson, 1981) modified by replacing crust model with that of AK135. Thin black dashed lines: Theoretical dispersion curves for models with identical crustal structure and different upper mantle velocities (constant 4.48, 4.4, 4.3, 4.2 km.s$^{-1}$) across 200 km thickness in the uppermost mantle. (b). Earth models Vs(z): Dashed black line: AK135. Solid black line: PREM. Blue line: starting model for Inversion 1. Solid green line: end model of Inversion 1. Solid red line: final model, which is the output model of Inversion 2. Dashed red lines: uncertainties of the resulting 1D shear wave velocity of Inversion 2.

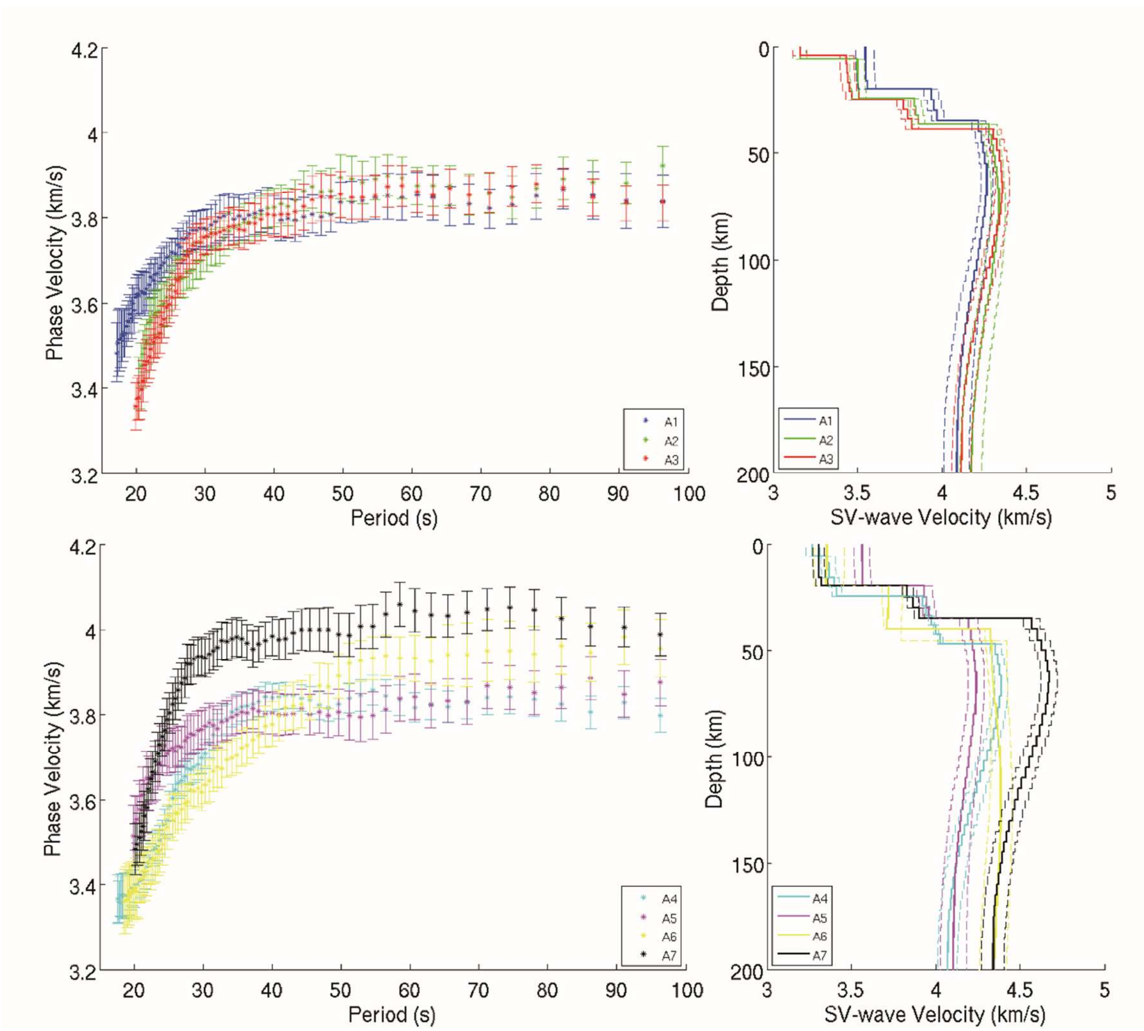


Figure 4. Dispersion curves (colored dots) and shear velocity models Vs(z) of the 7 large arrays

A1-A7. (a, b): Dispersion curves (fundamental mode Rayleigh waves). The colors refer to the array number, see also Figure 1. (c, d): Shear velocity Vs(z) as inferred from the dispersion curves in (a, b). Solid colored lines: the final model output model of Inversion 2, using the same color coding as in (a, b). Dashed colored lines: uncertainties of the resulting 1D shear wave velocity of Inversion 2.

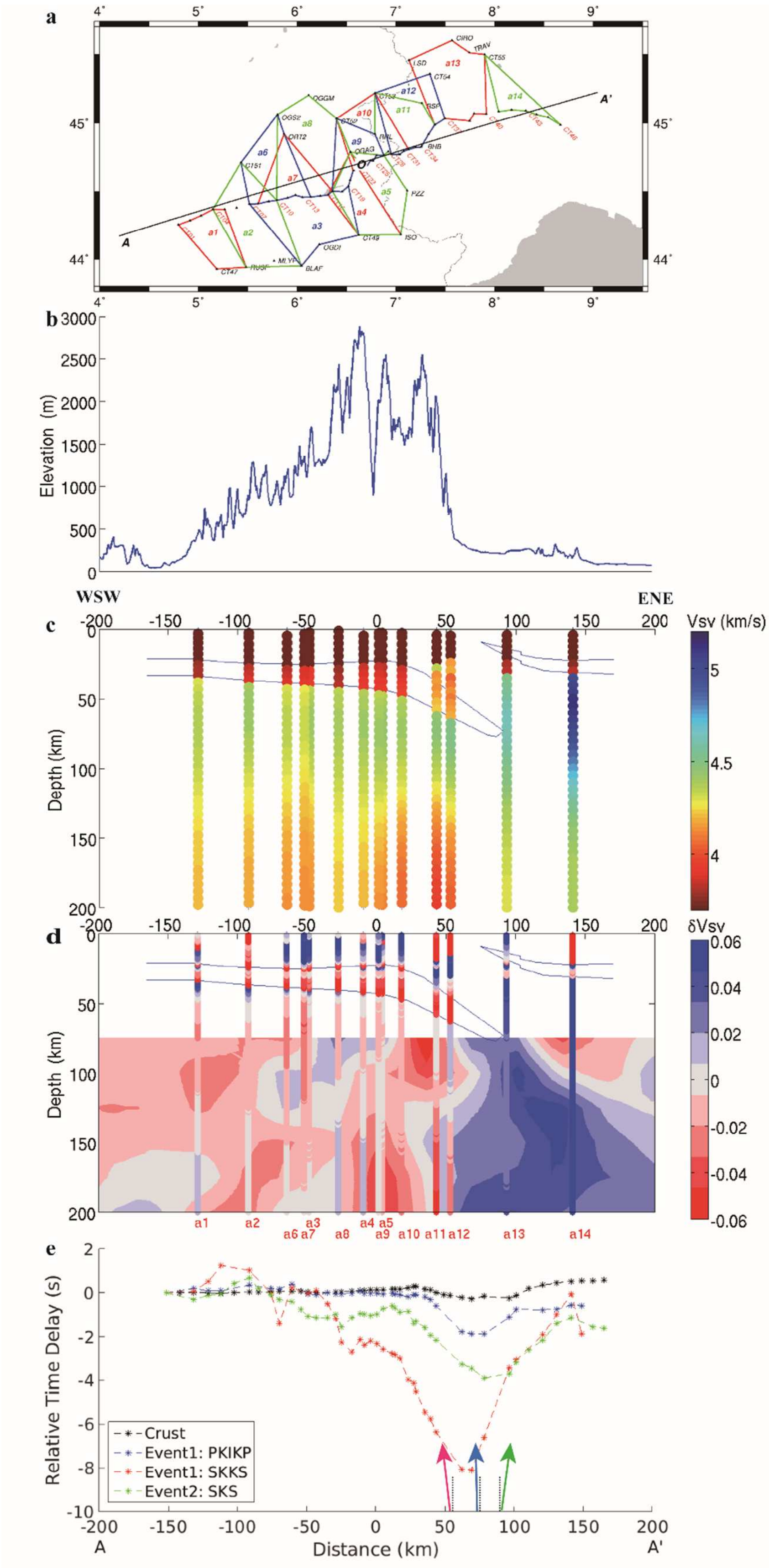
a
b
Elevation (m)
WSW
ENE
c
Depth (km)
Vsv (km/s)
d
Depth (km)
δVsv
a1
a2
a6 a7
a3
a8
a4 a5
a9 a10 a11 a12
a13
a14
e
Relative Time Delay (s)
Crust
Event1: PKIKP
Event1: SKKS
Event2: SKS
Distance (km)
A
A'

Figure 5. Vs model and relative body wave travel times. (a): Geometry of small arrays a1-a14. Station list for each array can be found in Supplementary Material, Table S1. (b): Topography along the profile AA'. (c): Absolute Vs along the CIFALPS profile AA' based on the results from 14 small arrays, each Vs profile projected onto the CIFALPS profile using the center of mass of the array. (d): Relative Vs. The perturbations are relative to the horizontal average calculated at each depth, i.e. relative to the average Vs(z) profile (see supplementary material Fig. S4). This representation corresponds to what is obtained by teleseismic body wave tomography, with the aim of comparing to the model by Zhao et al. (2016a), which is shown as the coloured background, using an identical color scale. (e): P and S relative time delays with respect to the westernmost stations for 2 events located approximately in the same azimuth as the CIFALPS reference profile (blue stars in Fig. 2). Event 1 was located at epicentral distance 170.5° towards the ENE of the CIFALPS profile. Two phases were observed for Event 1: PKIKP (blue line) with an incidence angle to vertical of 1.3° and SKKS (red line) with an incidence angle to vertical of 6.5°. Event 2 was located 92.6° towards the WSW of the CIFALPS profile. The analyzed phase, SKS (green line) has an incidence angle to vertical of 7.5°. The incidence to vertical is shown by the solid arrows. Relative time delays (with respect to the westernmost station) assuming vertical propagation within the crustal model of Zhao *et al*. (2015) and using a homogeneous mantle below, are shown as black stars.

# Supplementary Material

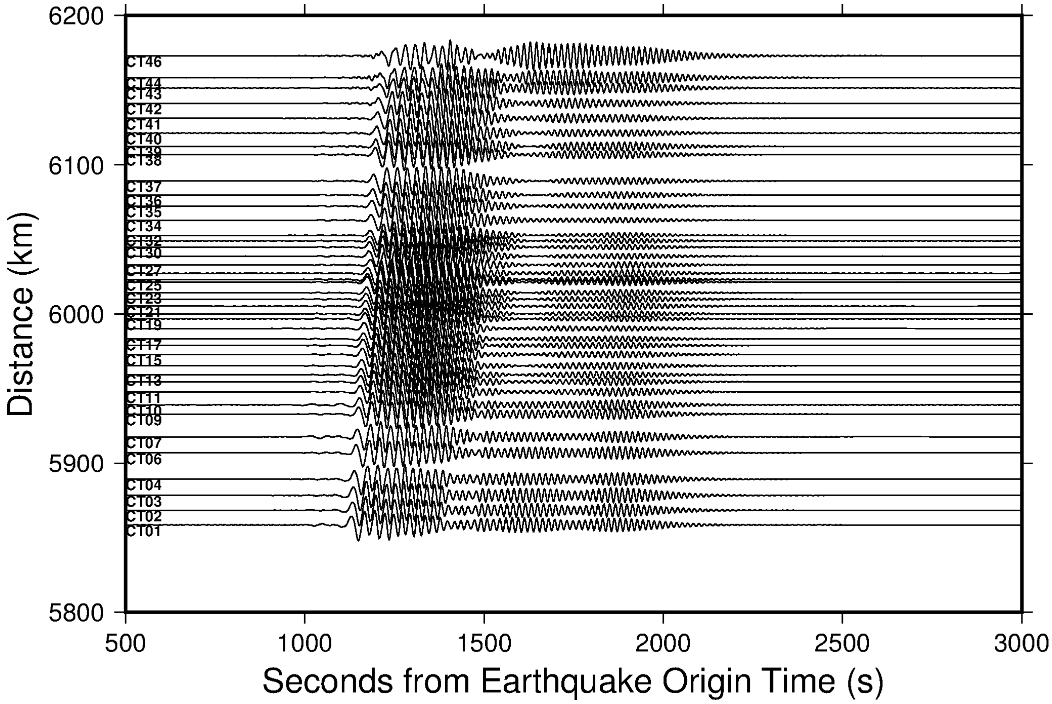


Figure S1. Vertical component records after the pre-processing of CIFALPS stations (CT01-CT46) along the profile AA' for the 2013 June 24, earthquake arriving approximately along the great-circle that goes through the profile.

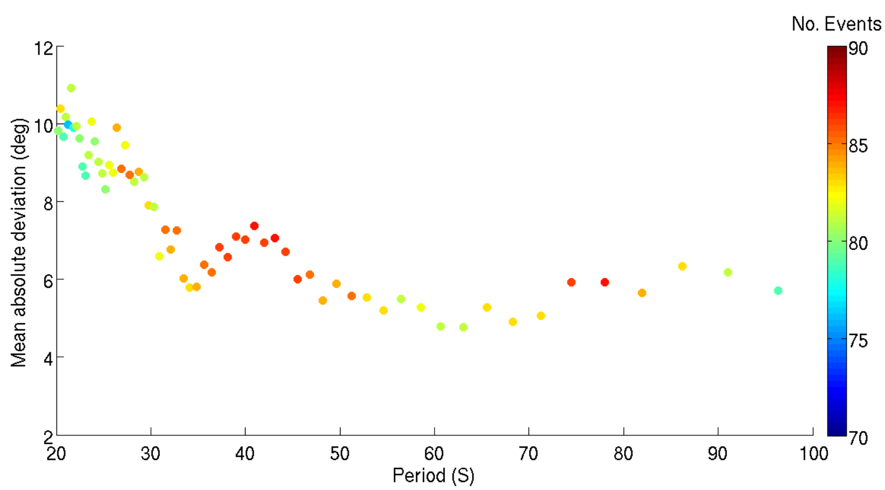


Figure S2. Mean absolute deviation (difference between observed arrival direction and the theoretical one as predicted for the center of the array) as a function of period. For each period, the colour of data points corresponds to the number of events contributing to the average. To stabilise the measurement, the arrival angle □$_k$(f) here is calculated by using all the stations in neighbouring arrays A1 and A2 which are located on similar crustal structures.

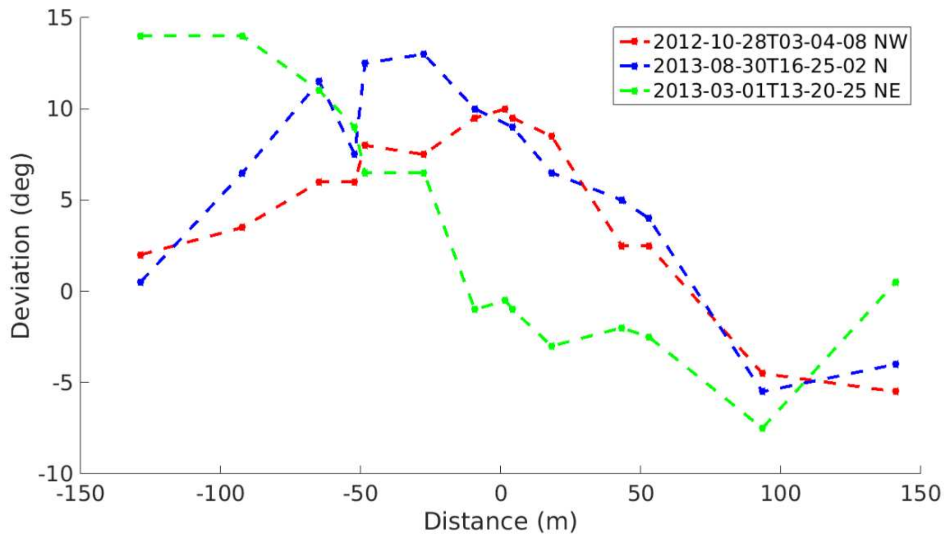


Figure S3. Azimuth deviations across the CIFALPS profile for three events, as observed using the 14 small arrays. The deviations are calculated as the difference between the observed arrival direction and the direction of the greatcircle as predicted for the center of mass of the array.

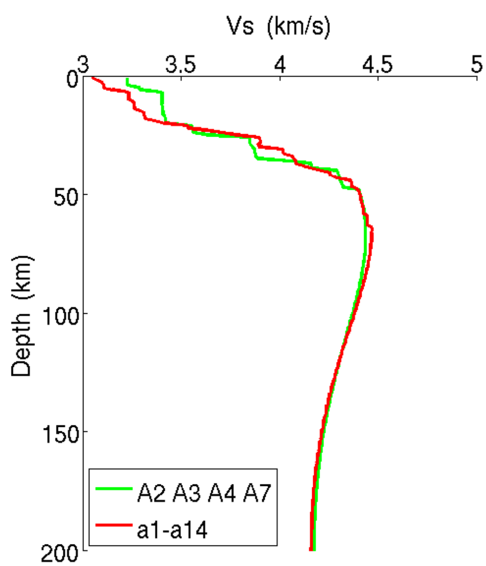


Figure S4. Average Vs(z). Red solid line: Shear velocity Vs(z) calculated as the average model for arrays a1-a14. This Vs(z) serves as reference profile for Fig. 5b. Green solid line:

Shear velocity Vs(z) calculated as the average model for arrays A2, A3, A4 and A7, which cover the approximately same geographical area as arrays a1-a14.

| **Large Arrays** | **Stations Distribution** |
|---|---|
| **A1** | SSB PY39 PY32 TRBF CT51 CT01 CT03 CT05 CT07 |
| **A2** | ARBF ARTF CT47 RUSF BSTF MLYF CT01 CT02 CT03 CT04 CT05 CT06 CT07 CT08 CT09 |
| **A3** | CT51 ORT2 CT52 OGAG CT07 CT08 CT09 CT10 CT11 CT12 CT13 CT14 CT15 CT16 CT17 CT18 CT19 CT20 CT21 CT22 CT23 |
| **A4** | PZZ CT50 CT52 OGAG CT53 RRL RSP CT54 CT23 CT24 CT25 CT26 CT27 CT28 CT29 CT30 CT31 CT32 |
| **A5** | CT49 PZZ CT50 ISO STV ENR CALF ESCA SAOF NEGI MON EILF |
| **A6** | OG35 OG02 RSL OGSM OGGM CT52 CT53 |
| **A7** | CT54 CT55 TRAV CIRO LSD SATI CT36 CT37 CT38 CT39 CT40 CT41 CT42 |

| **Small Arrays** | **Stations Distribution** |
|---|---|
| **a1** | CT47 RUSF CT01 CT02 CT03 CT04 CT05 |
| **a2** | RUSF BLAF CT51 CT04 CT05 CT06 CT07 CT08 CT09 CT10 |
| **a3** | OGDI BLAF CT49 CT07 CT08 CT09 CT10 CT11 CT12 CT13 CT14 CT15 CT16 CT17 CT18 CT19 |
| **a4** | CT49 OGAG ISO CT16 CT17 CT18 CT19 CT20 CT21 CT22 |
| **a5** | ISO CT49 PZZ OGAG CT17 CT18 CT19 CT20 CT21 CT22 CT23 CT24 CT25 CT26 CT27 CT28 |
| **a6** | CT51 ORT2 OGS2 CT07 CT08 CT09 CT10 CT11 CT12 CT13 CT14 |
| **a7** | ORT2 CT08 CT09 CT10 CT11 CT12 CT13 CT14 CT15 CT16 CT17 |
| **a8** | ORT2 CT52 OGS2 OGGM OGAG CT10 CT11 CT12 CT13 CT14 CT15 CT16 CT17 CT18 CT19 CT20 CT21 CT22 CT23 |
| **a9** | CT52 OGAG RRL CT17 CT18 CT19 CT20 CT21 CT22 CT23 CT24 CT25 CT26 CT27 |
| **a10** | CT52 CT53 OGAG RRL CT21 CT22 CT23 CT24 CT25 CT26 CT27 CT28 CT29 CT30 CT31 CT32 |
| **a11** | CT53 RRL RSP CT27 CT28 CT29 CT30 CT31 CT32 CT33 CT34 BHB CT35 CT36 |
| **a12** | CT53 CT54 RSP CT29 CT30 CT31 CT32 CT33 CT34 BHB CT35 CT36 CT37 |
| **a13** | CT54 CT55 TRAV CIRO LSD CT36 CT37 CT38 CT39 CT40 |

| | |
|---|---|
| **a14** | CT55 CT41 CT42 CT43 CT44 CT45 CT46 |

Table S1. Configuration of the arrays A1-A7 and a1-a14.